BiSON
Birmingham
Solar-Oscillations
Network

TECHNICAL REPORT NO. 385

Fibre-feed tests at Izaňa in 2017 September

Steven J. Hale

The University of Birmingham, Edgbaston, Birmingham B15 2TT

2017 September 29

This technical report series is published by:

High-Resolution Optical-Spectroscopy Group

THE UNIVERSITY
OF BIRMINGHAM

Fibre-feed tests at Izaña in 2017 September

Steven J. Hale

The University of Birmingham, Edgbaston, Birmingham B15 2TT

2017 September 29

Abstract

The new fibre-based spectrometer was updated from 2017 September 1 to 11. The detector electronic noise and atmospheric scintillation noise were both measured. The scintillation noise was found to be approximately 10^5 times higher than the electronic noise, and so the system is dominated by atmospheric noise. It is unlikely that the LCD-based system switching polarisation states at 5 Hz will be able to equal the performance of a typical Pockel's-cell-based system switching at 100 Hz. An overall reduction in noise power by a factor of almost 5 times is required to match the performance of Fred in Sutherland. This difference is of the order difference in scintillation noise between 5 Hz switching and 100 Hz switching.

Two fibre-feeds were trialled. A 30 mm focal length lens to replace the exiting 80 mm, and so focusing a smaller image of the Sun onto the end of the fibre, and a telescope arrangement coupling quasi-parallel light into the fibre. The shorter focal length lens resolves both the low- and high-frequency issues experienced since initial commissioning. The quasi-parallel telescope fibre-feed suffers some Doppler-imaging problems and also produces higher noise levels due to the lower light throughput.

The primary cœlostat mirror was replaced, and resulted in an increase in counts for Mark-I by approximately 3 %. The PMT HV-PSU was replaced, removing a temporary 2 kV unit and reinstating the normal 3 kV supply resulting in a further increase in counts for Mark-I by approximately 18 %.

Contents

1   Introduction

This is the second of a two-part report on a two-stage visit to Izaña. Steven Hale visited Izaña from 2017 September 1 to 11. The last visit to Izaña was in 2017 May to commission the

new fibre-based spectrometer [1]. The purpose of this visit was to investigate the cause of low-frequency issues and to test out two alternative optics for coupling sunlight into the fibre. Some general maintenance on Mark-I and the cœlostat was also carried out.

It is not intended that this technical report provide significant detail on the hardware design or the software controlling the new data acquisition system — this will be published in later reports. The intention of this trip report is only to log the work completed and to present the initial results of the performance tests. Section 2 looks at the electronic noise from the detectors and compares with the expected performance. Section 3 presents a log of the measured atmospheric scintillation noise on each day of the site visit, and data from a nearby ground-level dust sensor. Section 4 shows the data obtained each day using the two different fibre-feeds, and compares the performance with that expected from Sutherland. Finally, sections 5 and 6 log some general maintenance.

2 Electronic Noise

The noise performance of the new scattering detectors used in the BiSON Mini instrument has been simulated using SPICE, shown as the red line in Figure 1. To compare real performance with the simulation, noise from an isolated detector was captured with a Keysight InfiniiVision MSO-X 2012a oscilloscope.

The oscilloscope runs at several mega-samples per second and was configured to decimate to a total of 62 500 samples over a period of 0.5 s. This produces a final sampling rate of 125 kHz with 8 µs per sample, providing a 62.5 kHz Nyquist frequency limit. A total of 30 realisations of noise were captured in this configuration. For each realisation the Fourier transform was calculated and the amplitude spectral density determined, removing all phase information. Finally, the mean of all amplitude spectra was found in order to improve the signal to noise ratio in the absence of phase differences. The result is shown as the black line in Figure 1.

The physical detector suffers from some minor mains pickup at 50 Hz, and a peak around 30 kHz due to powering the detector from a switched-mode power-supply (SMPS), but broadly matches expectation. We can conclude that the detector is performing at the physical limit, and the only way to reduce the noise level is to either reduce the gain (brighter source) or reduce the size of the photodiode (higher shunt resistance, and lower capacitance).

The temperature control and data acquisition system was then powered on, and the test repeated. While care was taken in the detector design to ensure good grounding techniques and clean signal pathways, the attached data acquisition system does unfortunately induce additional noise in the scattering detector outputs. The majority of the additional noise is above 1 kHz, and increases noise RMS from 4.18 mV to between 7.2 mV (Figure 2) and 27.4 mV (Figure 3) depending on the CPU load. The transmission monitor, Figure 4, has much lower gain and so also a much lower noise level.

The additional noise does not impact as seriously on the final data as it might since the first stage of the data acquisition system, a 24-bit analogue to digital converter (ADC), includes a low-pass filter. In order to understand the output of the ADC we must first look briefly at the theory of operation. The data acquisition system is based around a number of Texas Instruments ADS1210 24-bit delta-sigma analogue to digital converters which are capable of data rates of several kHz [2], all read out via a Raspberry Pi single board computer. The ADS1210 is an integrated package containing a programmable gain amplifier (PGA), a second-order delta-sigma ($\Delta\Sigma$) modulator, a programmable digital low-pass filter, and a micro-controller
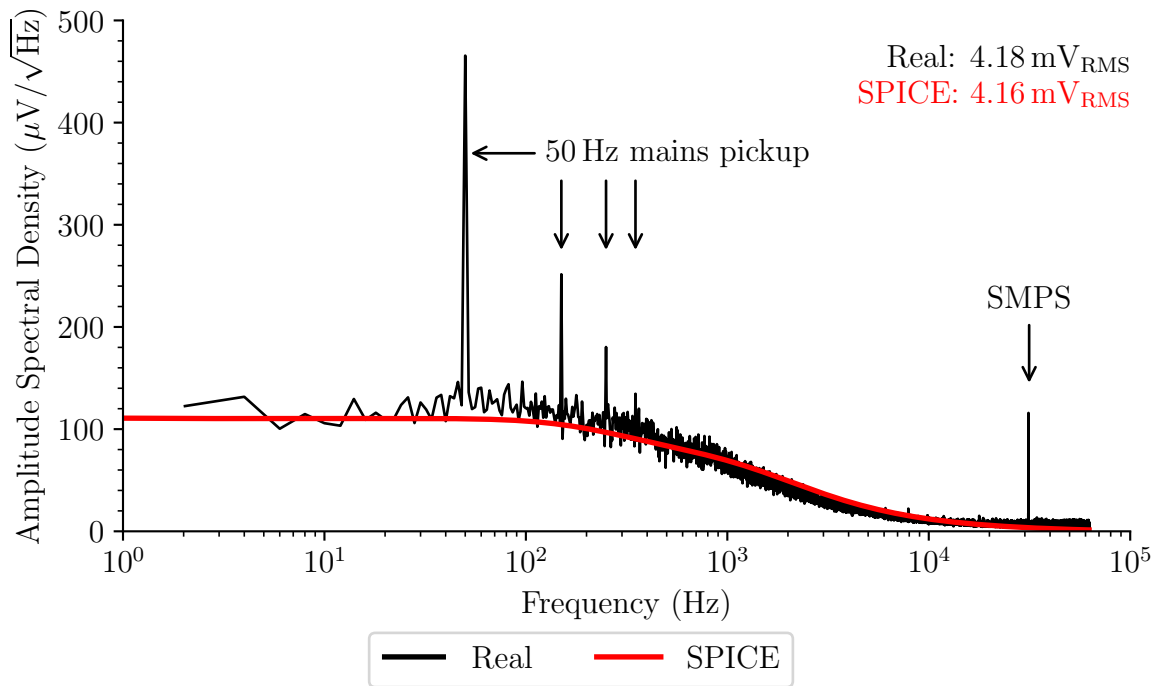
Figure 1: Measured detector noise, along with the expected noise profile from SPICE simulation. The physical detector suffers from some minor mains pickup at 50 Hz, and a peak around 30 kHz due to powering the detector from a switched-mode power-supply (SMPS), but broadly matches expectation.
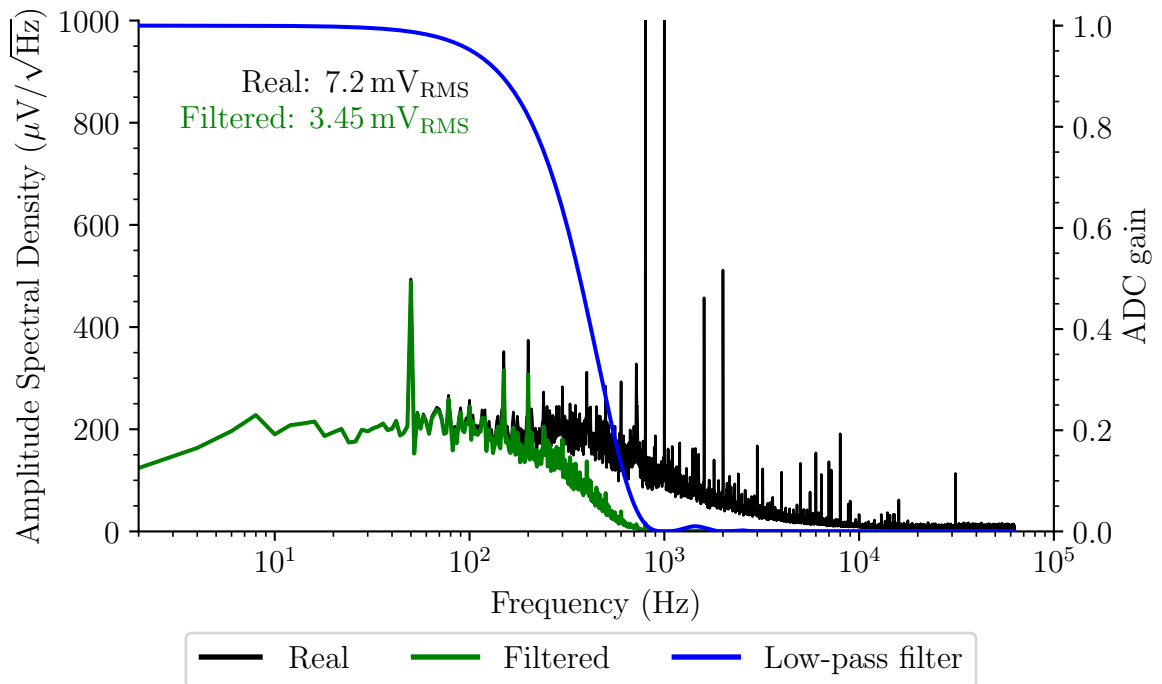

Figure 2: The black line shows the noise output from the detector when the temperature controller and Raspberry Pi are operating with low CPU load. The additional noise is predominantly caused by the Raspberry Pi and is above 1 kHz. The green line shows the detector output after passing through the low-pass filter stage of the ADC. The blue line shows the gain of the low-pass filter, measured against the right-hand axis.
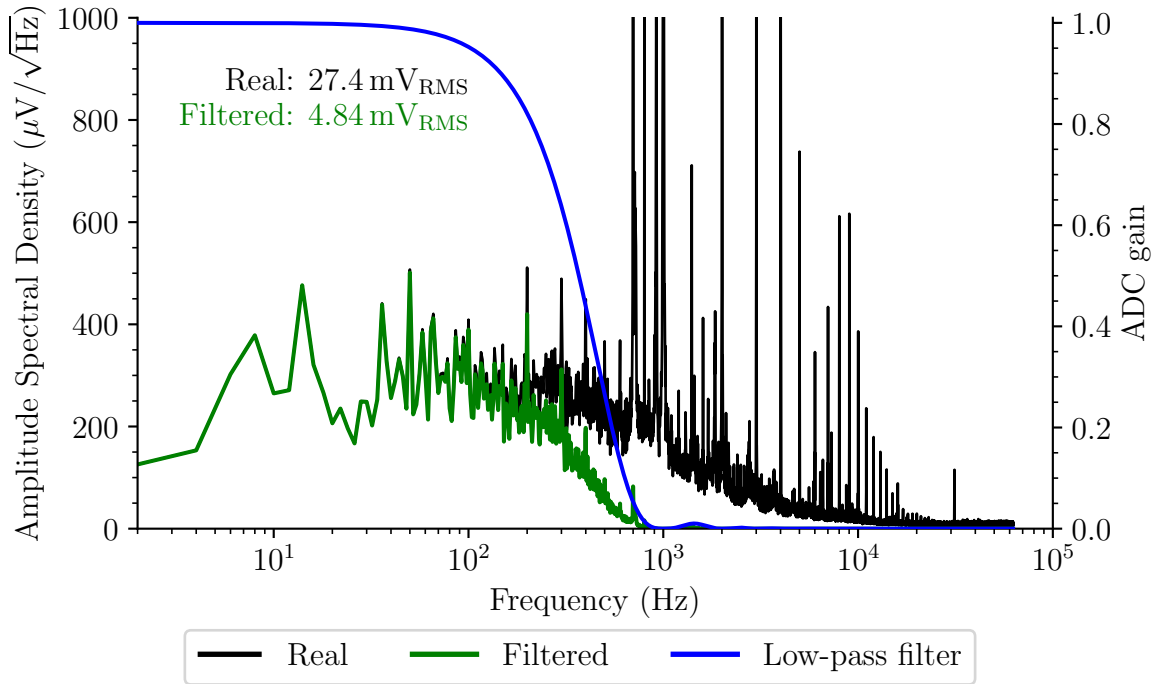
3

Figure 3: The black line shows the noise output from the detector when the temperature controller and Raspberry Pi are operating with high CPU load. The additional noise is predominantly caused by the Raspberry Pi and is above 1 kHz. The green line shows the detector output after passing through the low-pass filter stage of the ADC. The blue line shows the gain of the low-pass filter, measured against the right-hand axis.
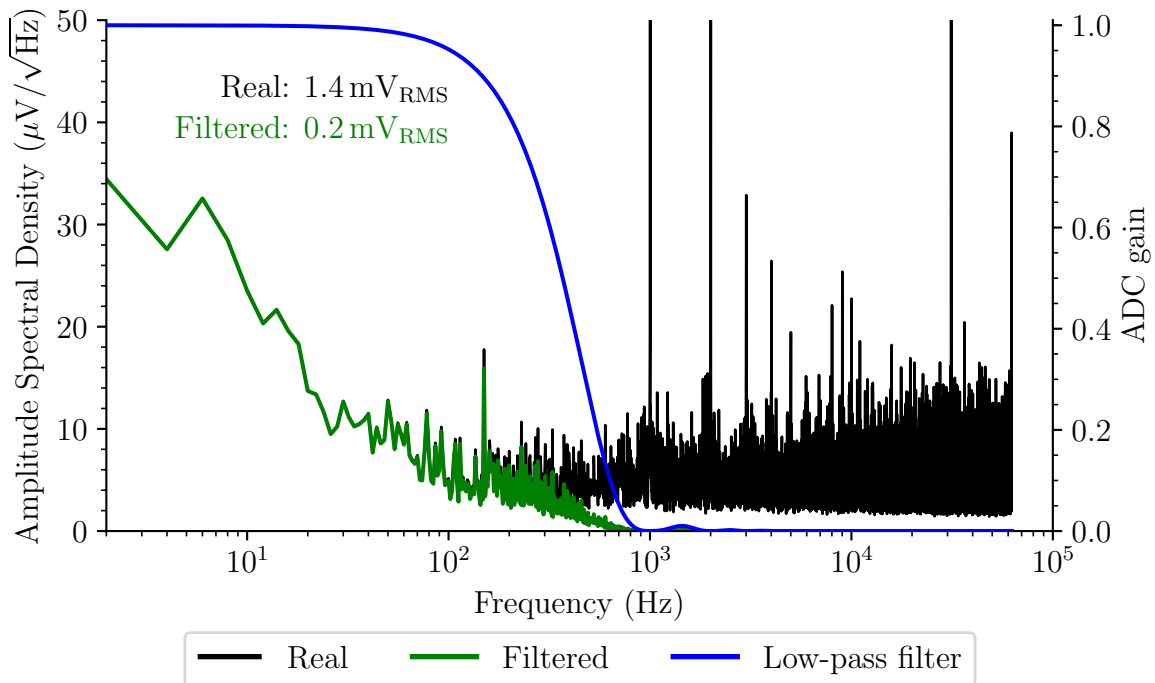

Figure 4: The black line shows the noise output from the transmission detector when the temperature controller and Raspberry Pi are operating. This detector has much lower gain than the scattering detectors, and so also a much lower noise level. The green line shows the detector output after passing through the low-pass filter stage of the ADC. The blue line shows the gain of the low-pass filter, measured against the right-hand axis.
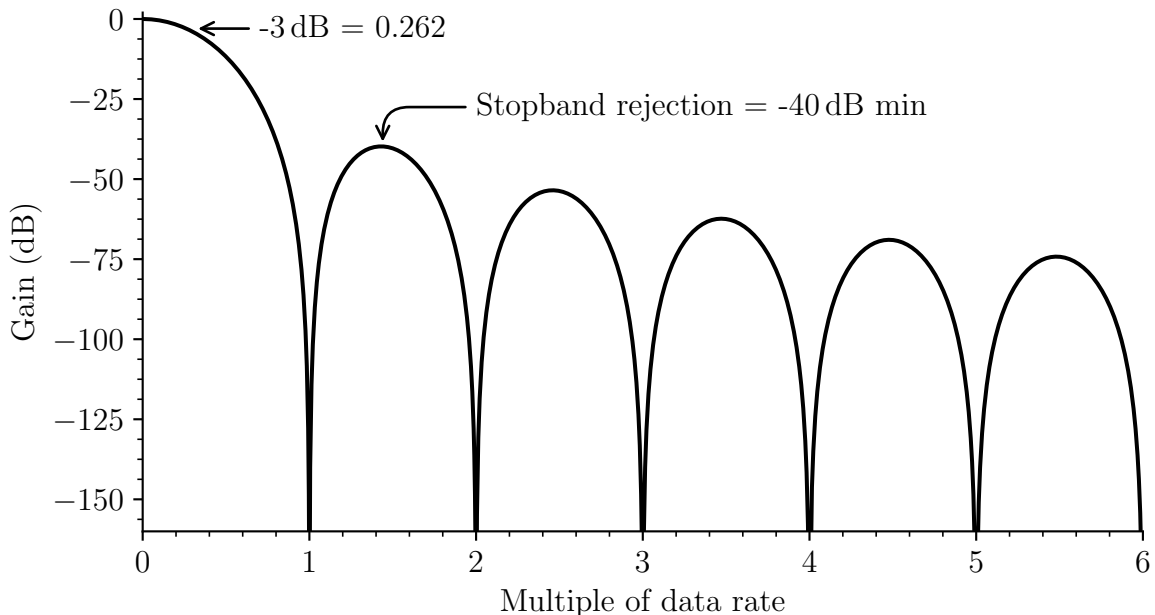
4

Figure 5: ADS1210 low-pass filter response. The $-3\,\mathrm{dB}$ point of the filter occurs at 0.262 times the data rate. Signals in the stopband, defined as frequencies higher than the first notch frequency at the data rate, have at least $-40\,\mathrm{dB}$ rejection.

with several control registers. The $\Delta\Sigma$ modulator is essentially a combined voltage-to-frequency converter and a pulse counter [3]. The modulator samples the incoming signal at a very high rate and converts it into a 1-bit stream of pulses by comparing the difference between the current input signal (the Δ) and passing it through an integrator (the Σ) and a comparator. A digital filter then reduces and converts the pulses into a high-resolution measurement of the input signal. This means that there are two sampling rates — the input sampling rate and the output data rate. The input sampling rate, f_{SAMP}, is defined by,

$$f_{\mathrm{SAMP}} = \frac{\mathrm{TMR} \cdot \mathrm{PGA} \cdot f_{\mathrm{XIN}}}{512} \ , \tag{1}$$

where f_{XIN} is the frequency of the crystal oscillator controlling the main clock of the ADS1210, PGA is the multiplier of the programmable gain amplifier, and TMR is the turbo mode rate multiplier which can boost the sampling rate for higher precision. The ADC is installed with a $5\,\mathrm{MHz}$ crystal, the TMR is set to the maximum 16 times multiplier, and the PGA set to the minimum unity-gain. This produces an input sampling rate of $156.25\,\mathrm{kHz}$. By oversampling at a rate much higher than the band of interest, the quantisation noise is pushed up to higher frequencies and then removed by the low-pass decimation filter producing an effect known as noise shaping. The effectiveness of noise shaping can be improved by using multiple integrators. The ADS1210 uses a second-order modulator with two integrators meaning that the noise term depends on the previous two errors rather than just one.

The output data rate, f_{DATA}, and the bandwidth of the digital low-pass filter are both determined by the decimation ratio [4]. The output data rate can be calculated from,

$$f_{\mathrm{DATA}} = \frac{\mathrm{TMR} \cdot f_{\mathrm{XIN}}}{512 \cdot (N+1)} \ , \tag{2}$$

where N is the decimation ratio. For the ADS1210, valid decimation ratios range from 19 to 8000. If values are defined outside of this range then the digital filter will have either not

enough, or too much, data resulting in incorrect results. By rearranging equation 2 we can determine the required decimation ratio for the desired data rate,

$$N = \frac{\text{TMR} \cdot f_{\text{XIN}}}{512 \cdot f_{\text{DATA}}} - 1 \ , \tag{3}$$

where terms are as defined before. Lower decimation ratios produce higher data rates with higher bandwidth, and as such include more quantisation noise. Lower data rates provide better signal-to-noise ratio and so increase the effective-number-of-bits (ENOB) of the ADC. The digital filter used by the ADS1210 has a $(\sin(x)/x)^3$ response known as a sinc^3 filter, and it is described by the following transfer function,

$$|H(f)| = \left| \frac{\sin\left(\frac{\pi f N}{f_{\text{MOD}}}\right)}{N \sin\left(\frac{\pi f}{f_{\text{MOD}}}\right)} \right|^3 \ , \tag{4}$$

where N is again the decimation ratio, f_{MOD} the frequency of the $\Delta\Sigma$ modulator, and f the input signal frequency. Figure 5 shows the frequency response in terms of multiples of the data rate. The $-3\,\text{dB}$ point of the filter occurs at 0.262 times the data rate. Signals in the stopband, defined as frequencies higher than the first notch frequency at the data rate, have at least $-40\,\text{dB}$ rejection. A $1\,\text{kHz}$ data rate requires a decimation ratio of 155 which is within the valid range allowed by the ADS1210, and produces a low-pass filter response with the $-3\,\text{dB}$ point at $262\,\text{Hz}$.

When this filter is applied to the output from the scattering detectors, shown as the green line in Figure 3, the noise RMS reduces from $27.4\,\text{mV}$ to $4.84\,\text{mV}$ which is close to the original clean output of the isolated detector. Whilst the low-pass filter removes most of the noise induced by the Raspberry Pi, it would be better if the source of the noise could be eliminated. When the filter is applied to the clean detector output the noise RMS reduces to $2\,\text{mV}$, and so there is potential for a factor of 2.4 reduction in the electronic noise level with further work in addition to that achievable by changes in gain and photodiode model.

3   Atmospheric Scintillation

The new spectrometer prototype uses an LCD retarder to switch between circular polarisation states, rather than the Pockel's-effect cell typically installed in our existing spectrometers. The advantages to this component change are that commercial off-the-shelf controllers are readily available, and they operate at much lower voltages — typically $\pm 25\,\text{V}$ rather than $\pm 3\,\text{kV}$. Unfortunately a major downside is that they are much slower to change polarisation states. A Pockel's cell can switch between left and right quarter-wave retardance in well under $1\,\text{ms}$, whereas an LCD retarder takes upwards of $20\,\text{ms}$. This means that the polarisation switching rate used with LCDs needs to be reduced from the typical $100\,\text{Hz}$ down to the order of $5\,\text{Hz}$ while still maintaining a reasonable percentage of dead-time per acquisition period.

Since the polarisation state switching is slower, atmospheric turbulence will have a larger impact on the data noise level. Izaña also suffers from periods of reduced visibility due to wind-borne Saharan dust. There are a number of telescopes providing weather information at the IAC. The STELLA Robotic Observatory provides several environmental parameters, and usefully one of these is a dust sensor [5] with records dating back to early 2009. The values from the dust sensor are used by the observatory, but there seems to be little known about the make or model of the sensor or how it works. A walk down to the STELLA site revealed a VisGuard 2 In-situ Visibility Monitor [6] manufactured by SIGRIST Process-Photometer, a Swiss company. The

Table 1: Qualitative dust limits used at the IAC.

Qualitative Dust Measurement		Range (m^{-3} PLA)	
Spanish	English	Min	Max
Poca	Little		<0.0025
Media	Half	0.0025	<0.0100
Bastante	Quite	0.0100	<0.0175
Mucha	A lot	0.0175	<0.0250
Fuera limites	Outside limit	0.0250	
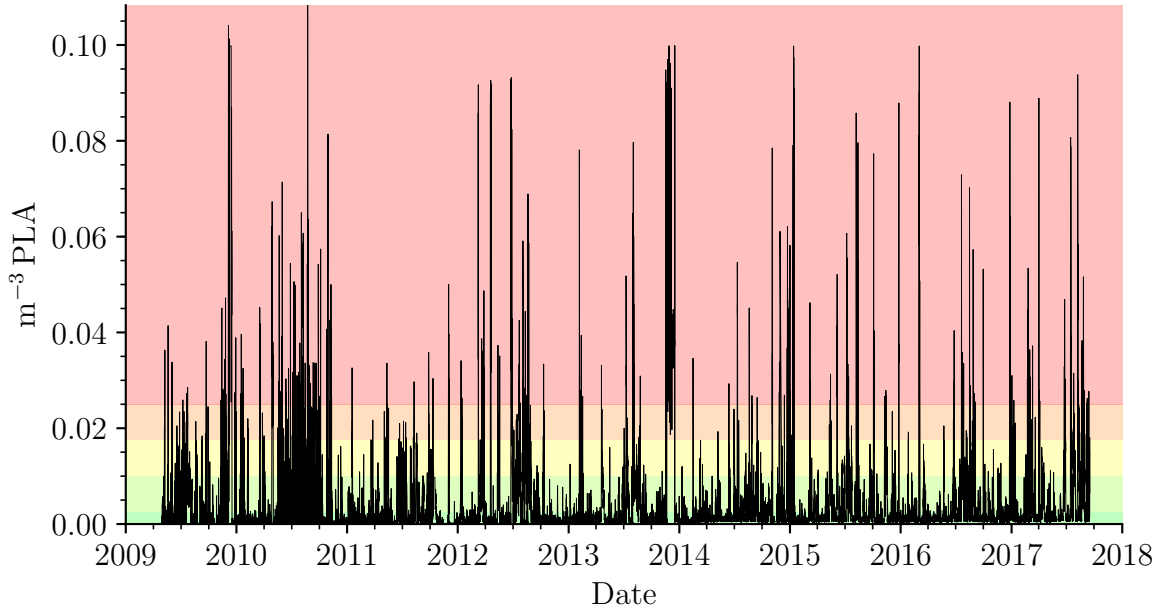
Figure 6: Dust data from the STELLA telescope. The coloured bands indicate the qualitative limits described in Table 1.
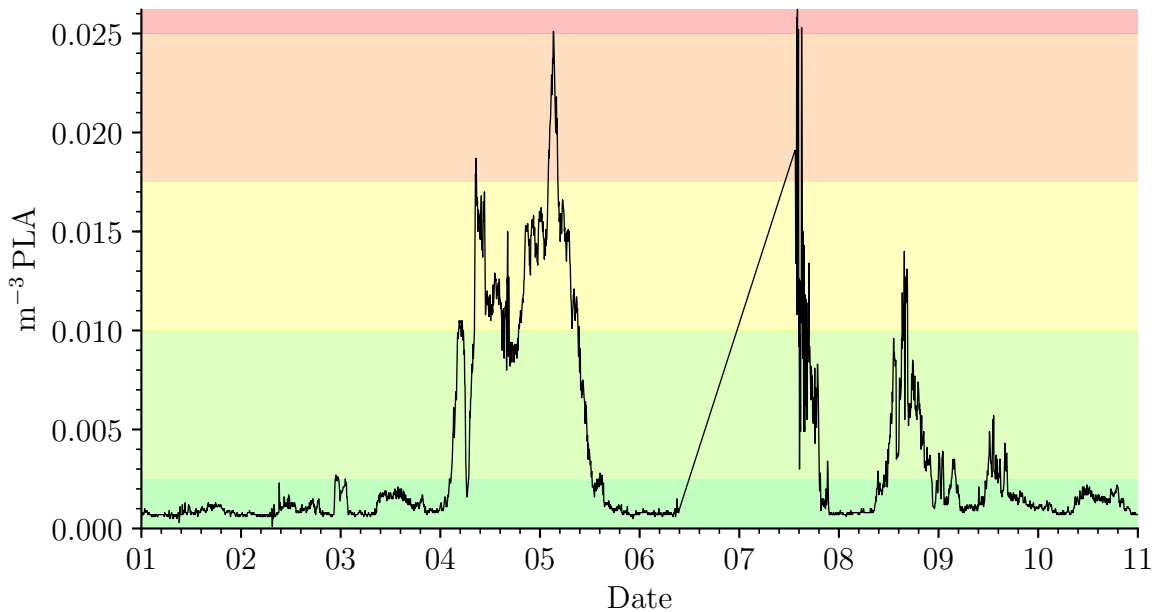
Figure 7: Dust data from the STELLA telescope for the duration of this site visit. The coloured bands indicate the qualitative limits described in Table 1.
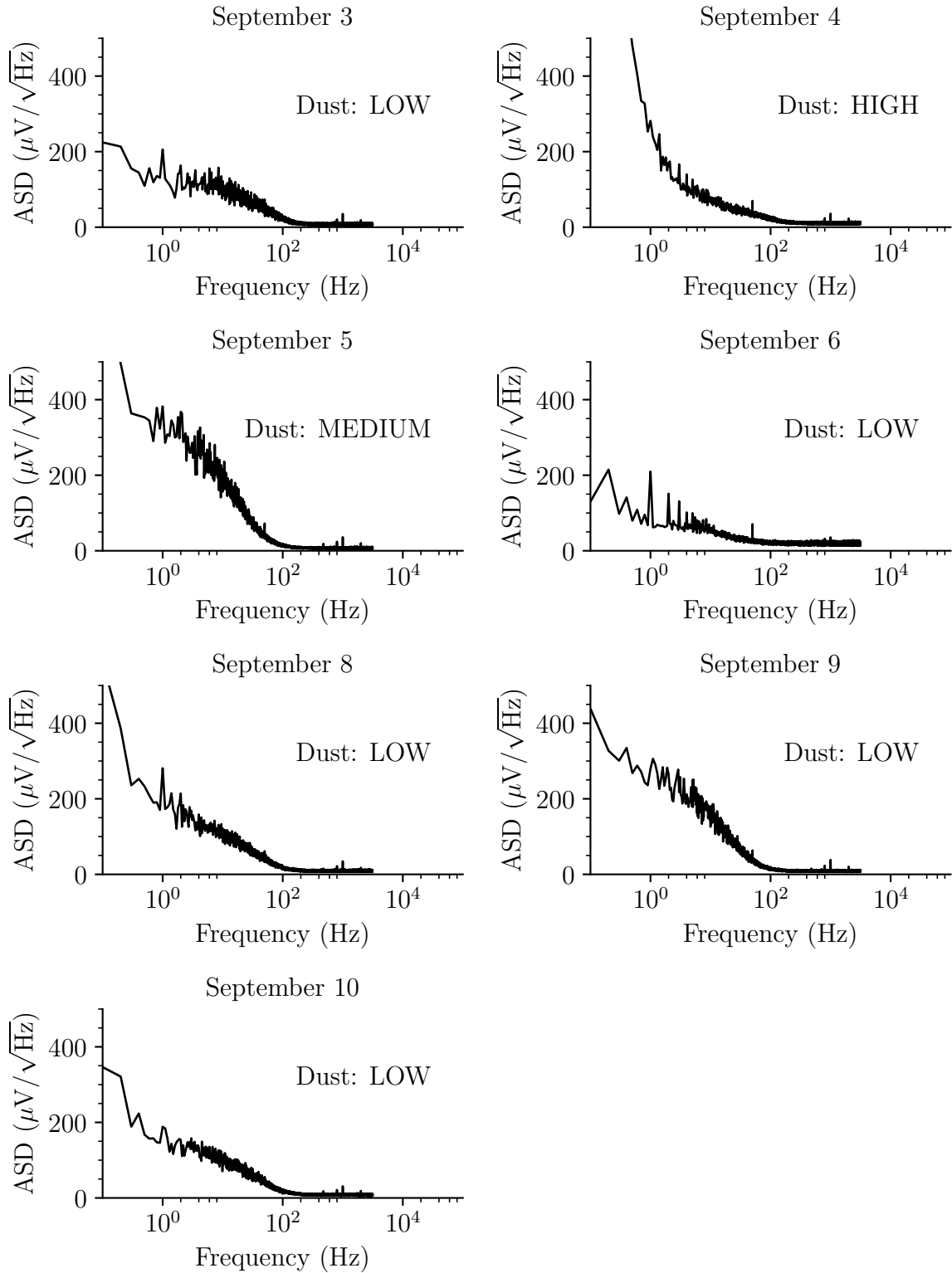
7

Figure 8: Daily scintillation measurements.

datasheet for the product along with the SIGRIST Visibility Measurement glossary [7] details how it works.

The VisGuard is a device intended for use in vehicle tunnels to monitor visibility and carbon monoxide concentration, and used to control the ventilation system to minimise energy use or close the tunnel if limits are exceeded. It is also used as an early warning system for fires. The VisGuard is essentially a photometer that measures the intensity of scattered light from an air sample drawn into the instrument by a fan, meaning that the measurement is taken at ground level and not at altitude. The operation is much the same as our own spectrometers.

The photometer illuminates the sample at a wavelength of 880 nm and compares the light scattered at a 30° angle with the directly transmitted light. This two-beam system eliminates effects due to temperature, aging of the electronics, or fluctuation of the light source. The output is a measure of Polystyrol-Latex-Aerosols (PLA) which is then multiplied by some factor to obtain the extinction coefficient. For example, for use in tunnels the PLA is multiplied by 30 to produce extinction per metre (E/m). The STELLA web page provides values in terms of PLA per cubic-metre. However, in terms of dust measurement the absolute value is not particularly important so long as we have some qualitative idea of what is considered low and what is considered to be high. The IAC have defined some threshold levels, and these are detailed in Table 1. The data from the sensor is shown in Figure 6 with coloured banding from green to red to indicate the threshold levels. Figure 7 shows the dust measurements during the period of this site visit. It is possible to estimate the true extinction coefficient due to aerosols through an entire column of the atmosphere (as opposed to only ground level) by fitting the measured solar intensity against the expected airmass for the solar zenith angle [8].

In order to determine the effects of the reduced switching rate, an attempt was made to measure atmospheric scintillation noise. This was done in much the same was as measuring the detector electronic noise in Section 2. With the polarisation switching disabled, data from the transmission monitor was logged for 10 s at 6.25 kHz. A total of 24 realisations of noise were captured in this configuration, making two minutes of data in 10 s chunks. From each 10 s chunk the amplitude spectral density was calculated and then stacked to improve the final signal to noise ratio. This was done at approximately the same time each day during periods of varying atmospheric stability, and the results are shown in Figure 8

Both the electronic noise from the scattering detectors, and low-dust atmospheric scintillation measured at the transmission monitor, produce typical values of $200\,\mu V/\sqrt{Hz}$. If these values are rescaled to compensate for the different detector gains then the noise equivalent power (NEP) can be calculated. This is the equivalent signal that would be required to produce the same output from an ideal noiseless detector.

The scattering detectors have a first stage transimpedance amplifier with a $100\,M\Omega$ gain resistor, followed by a second stage inverting voltage amplifier with 30.9 times gain. The photodiode has a responsivity at 770 nm of approximately $0.45\,A\,W^{-1}$. The electronic NEP is $0.14\,pW/\sqrt{Hz}$.

The transmission monitor has a first stage transimpedance amplifier with a $30\,k\Omega$ gain resistor, followed by a unity-gain inverter. The scintillation NEP is $14.8\,nW/\sqrt{Hz}$. This is over 10^5 times higher than the electronic noise, and so the system is dominated by atmospheric noise. It is unlikely that we will be able to achieve the same performance as our other instruments switching at 100 Hz.

4   Data Quality

Two new fibre-feeds were trialled. The existing 80 mm objective lens focuses an image of the Sun onto the end of the fibre that is almost the exact diameter of the fibre itself. This is thought to be causing the low- and high-frequency issues experienced since initial commissioning. The first new fibre-feed is a 30 mm focal length lens focusing a smaller image of the Sun onto the end of the fibre. The second is a telescope arrangement of an 80 mm focal length objective lens and a 10 mm focal length "eyepiece" lens coupling quasi-parallel light into the fibre. The idea is that the telescope arrangement should reduce or eliminate issues involving placing an image on the end of the fibre, such as dirt causing vignetting of the solar disc, and guiding problems.

Figures 9 to 18 show the daily data collected during this site visit. Figure 19 compares data from the best day, 2017 September 10, with data from both the Mark-I spectrometer and Fred in Sutherland. All data were collected using the 30 mm lens fibre-head, except for the afternoon of 2017 September 5 (Figure 13) and the whole of 2017 September 6 (Figure 14) which were collected using the quasi-parallel telescope arrangement. These two days show a noticeably higher noise level due to the lower light throughput and efficiency of coupling to the fibre. There also appears to be some Doppler-imaging issues that are not present when using the simple 30 mm lens.

The figure-of-merit (FOM) calculated by Red is different from the values presented in the recent network performance paper [9]. Red calculates the ratio of the mean power in the five minute band (2 mHz to 5 mHz) to the mean power in the high frequency noise (5.5 mHz to 12.5 mHz). The values in the performance paper are calculated using the total power in the five minute band and the total power in the high frequency noise, and so the values from Red are higher by a factor of 7/3 due to the differences in bandwidth of the two regions. There are other smaller variations in value due to the algorithm used to transform from the time domain to the frequency domain. Red calculates a Lomb normalised periodogram as described by Press et al. [10]. In the performance paper, and here, we calculate the standard Cooley–Turkey discrete Fourier transform [11] as implemented in the Python NumPy library.

On 2017 September 10, Mark-I achieves a FOM of 3.4. The mean noise in the 10 mHz to 12.5 mHz band is $53.6\,(\mathrm{ms^{-1}})^2\,\mathrm{Hz^{-1}}$. If we assume this is the background noise level for the whole spectrum, then this corresponds to an RMS in the time domain of $81.9\,\mathrm{cm\,s^{-1}}$. On the same day, the new instrument achieves a FOM of 14.6. The mean noise in the 10 mHz to 12.5 mHz band is $6.8\,(\mathrm{ms^{-1}})^2\,\mathrm{Hz^{-1}}$, corresponding to an RMS in the time domain of $29.2\,\mathrm{cm\,s^{-1}}$. For comparison, the same day from Fred in Sutherland achieves a FOM of 46.2. The mean noise in the 10 mHz to 12.5 mHz band is $1.4\,(\mathrm{ms^{-1}})^2\,\mathrm{Hz^{-1}}$, corresponding to an RMS in the time domain of $13.3\,\mathrm{cm\,s^{-1}}$. While the modifications to the new instrument have improved the results from the earlier tests in May, we still need to achieve a reduction in noise power by a factor of almost five to match the performance of Fred in Sutherland. This difference is of the order difference in scintillation noise between 5 Hz switching and 100 Hz switching.

5   Primary Mirror Replaced

The primary cœlostat mirror was replaced at 11:30 on 2017 September 7, and the original mirror was taken for cleaning. There was little visible difference between the two mirrors. The change resulted in an increase in counts for Mark-I by approximately 3 %, and for Mini by almost 4 %.
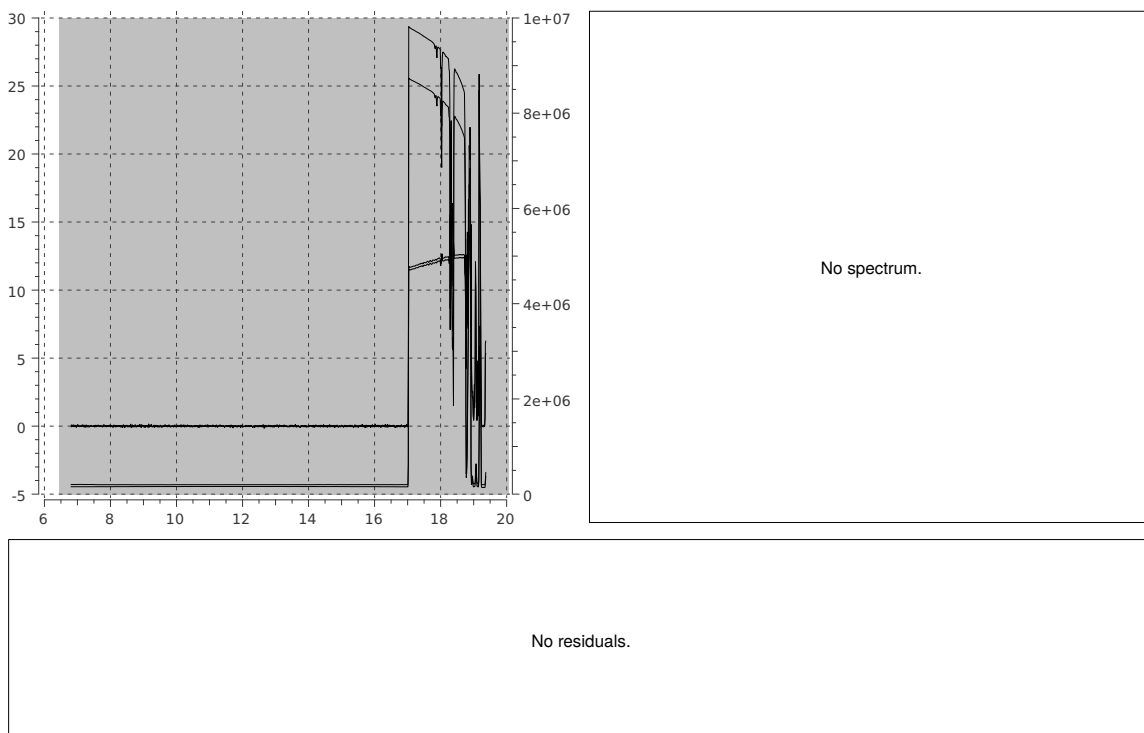
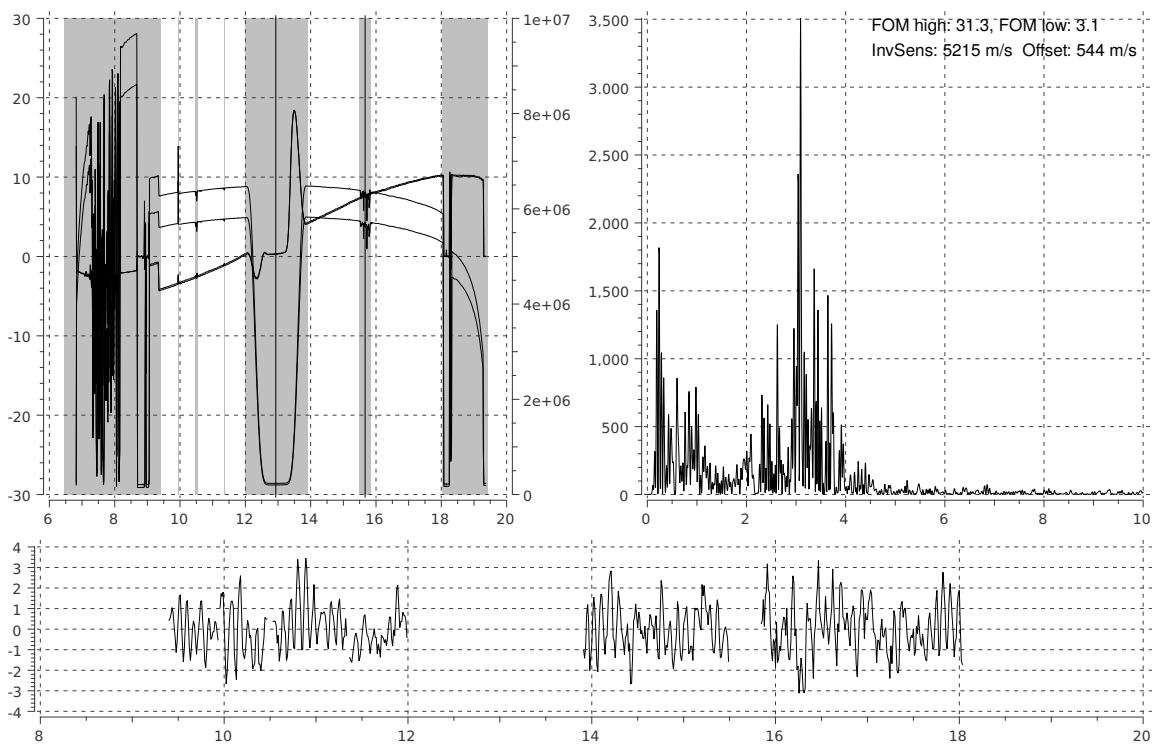**Figure 9**: 2017 September 1

Figure 10: 2017 September 2

11

Izana/Mini - 2017 September 3
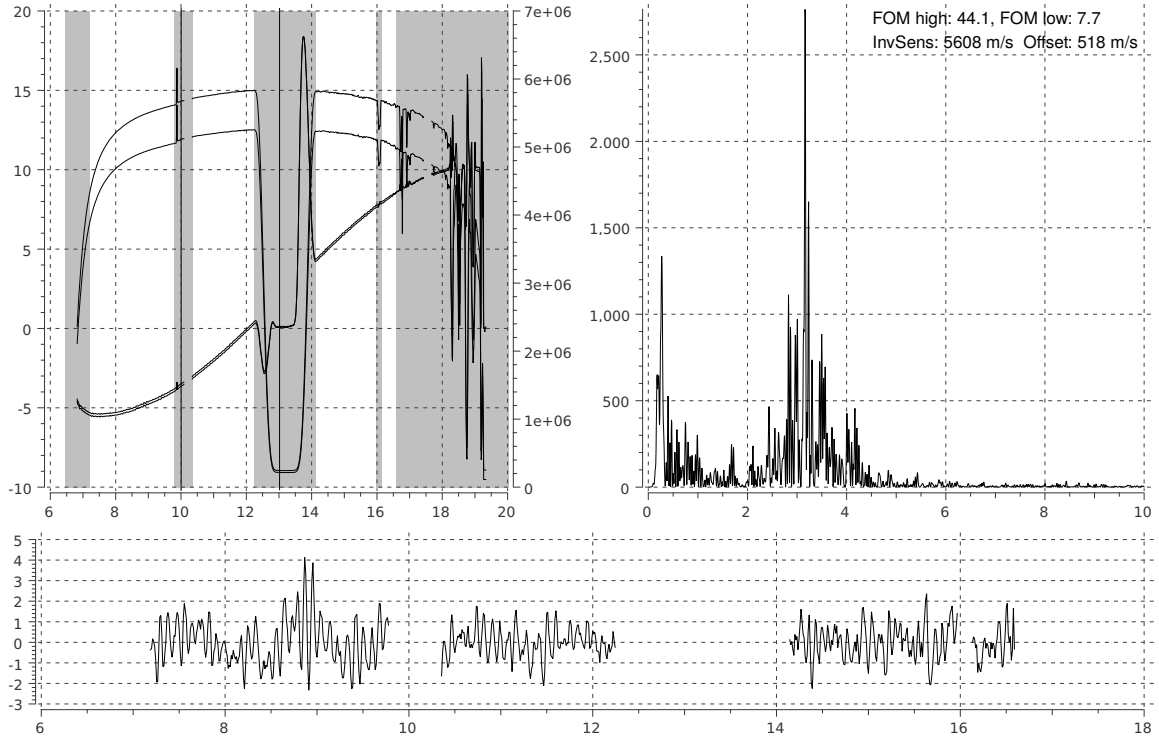

Figure 11: 2017 September 3
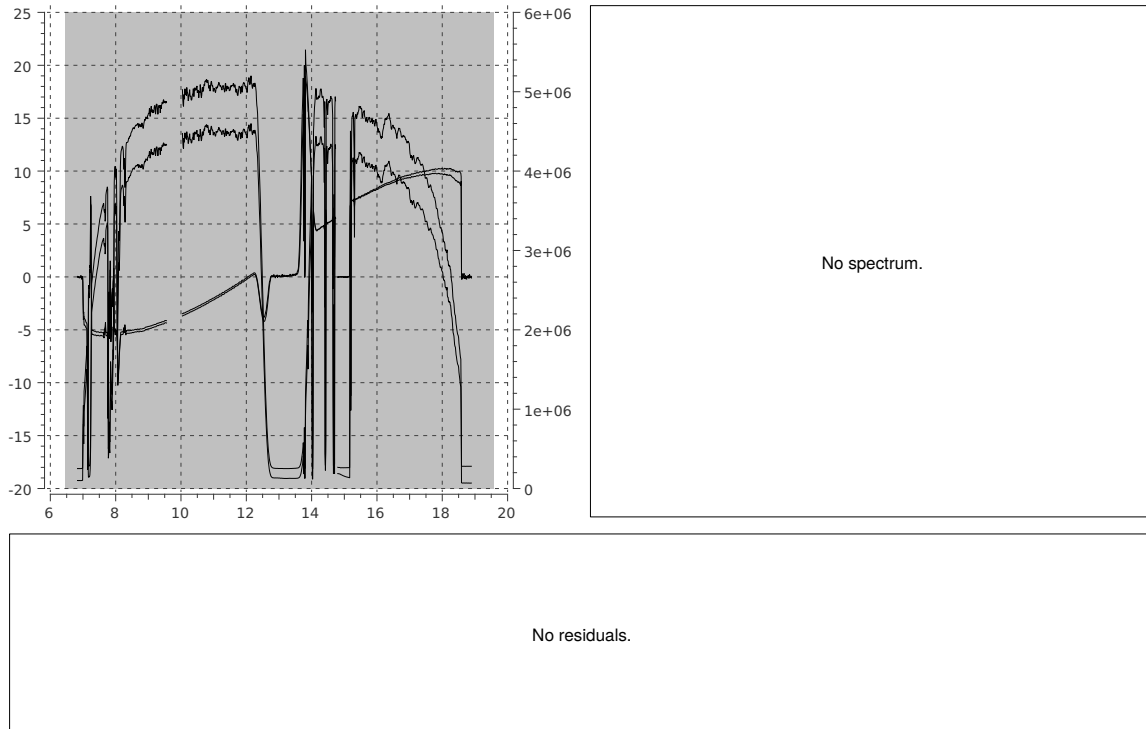
Izana/Mini - 2017 September 4

Figure 12: 2017 September 4

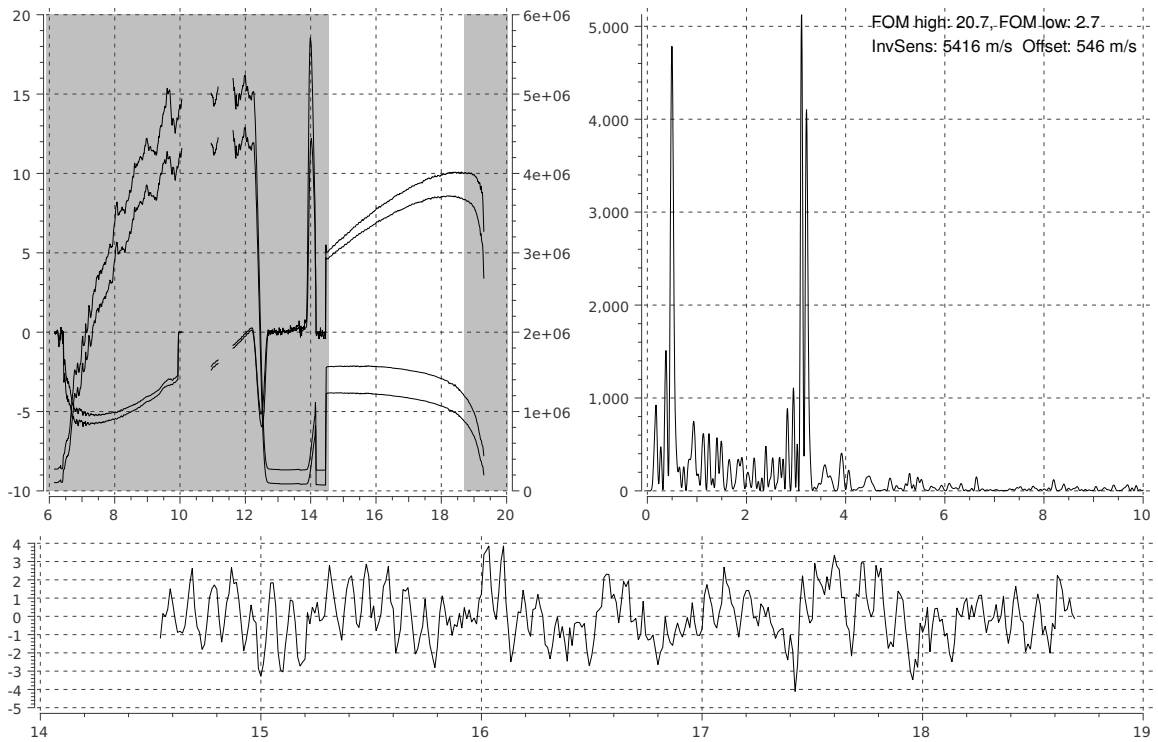**Izana/Mini - 2017 September 5**

Figure 13: 2017 September 5. The second half of this day was collected using the quasi-parallel telescope arrangement.
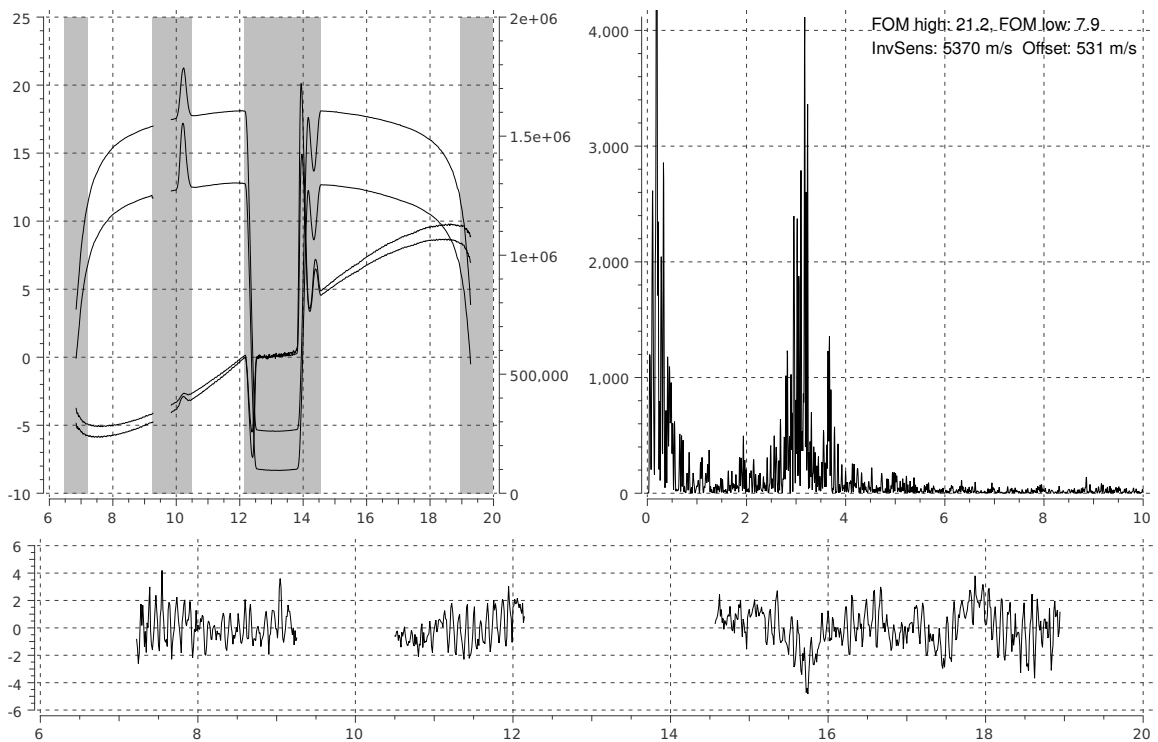
Izana/Mini - 2017 September 6

Figure 14: 2017 September 6. This day was collected using the quasi-parallel telescope arrangement.
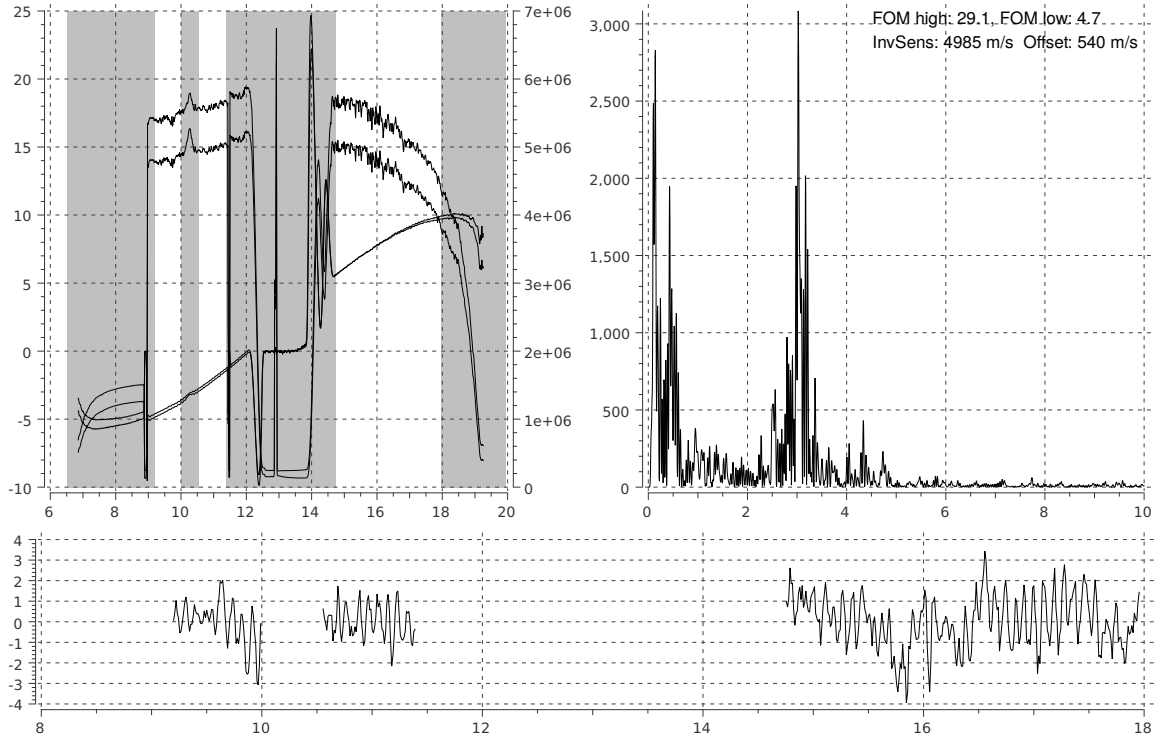
13

Izana/Mini - 2017 September 7

FOM high: 29.1, FOM low: 4.7
InvSens: 4985 m/s Offset: 540 m/s

Figure 15: 2017 September 7

Izana/Mini - 2017 September 8

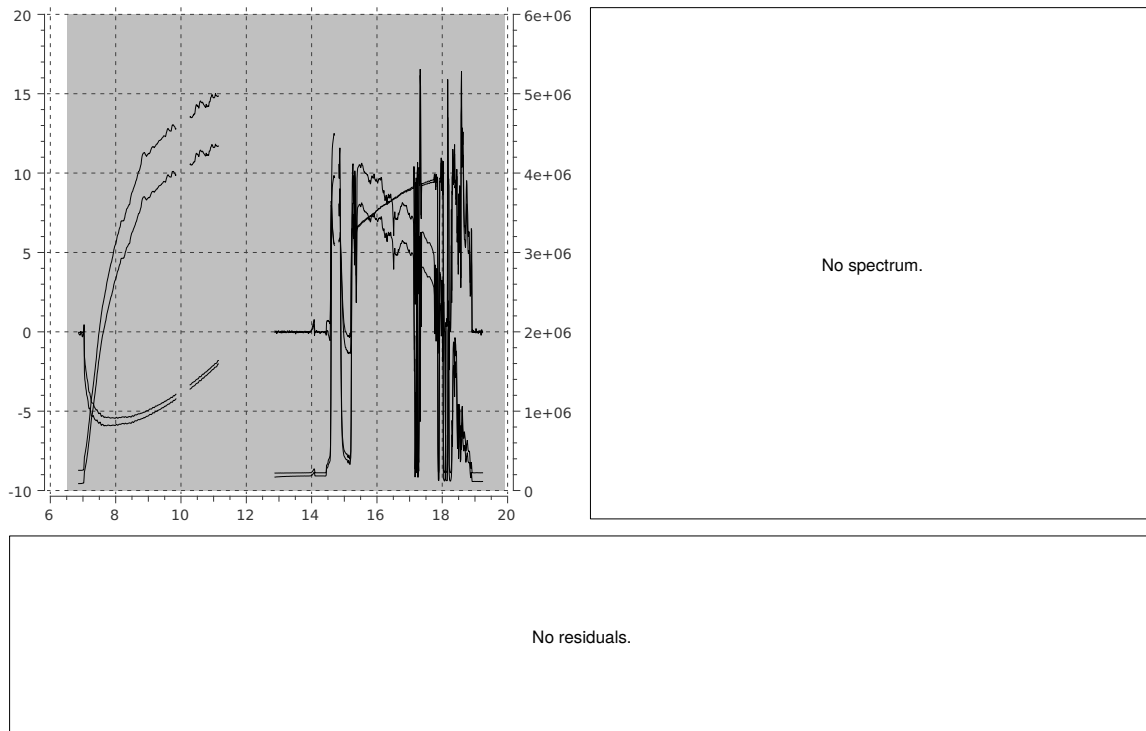No spectrum.

No residuals.

Figure 16: 2017 September 8
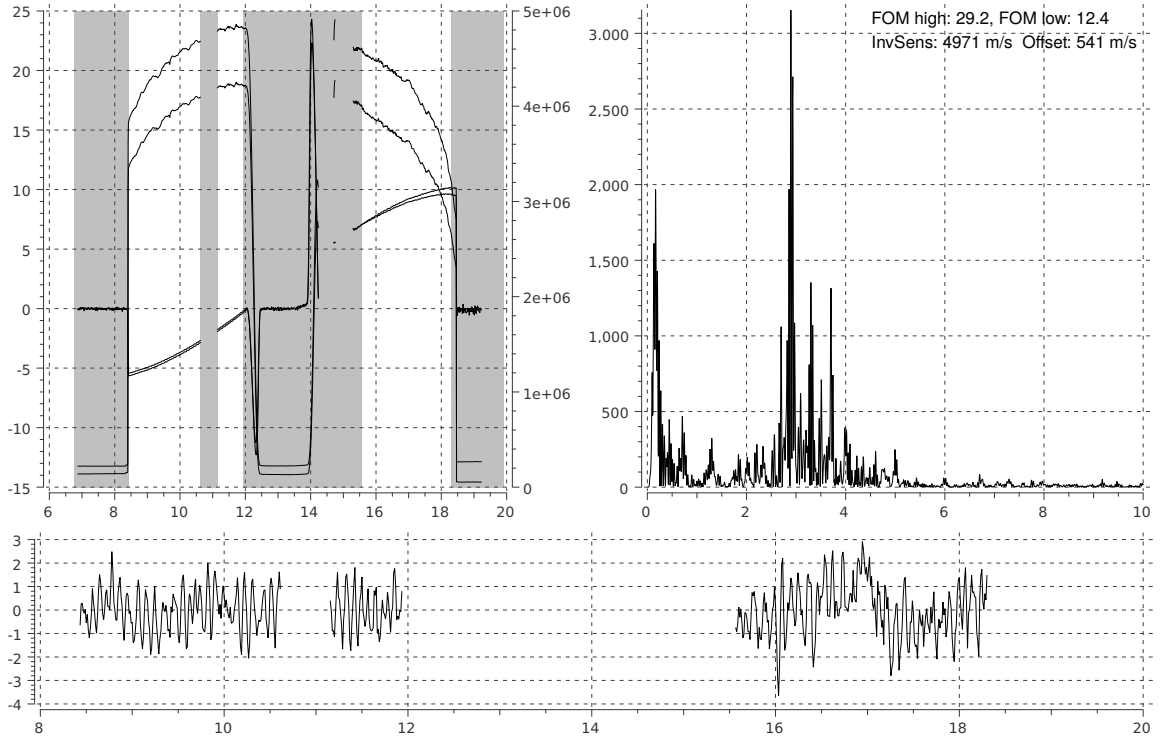
14

Izana/Mini - 2017 September 9

Figure 17: 2017 September 9

Izana/Mini - 2017 September 10
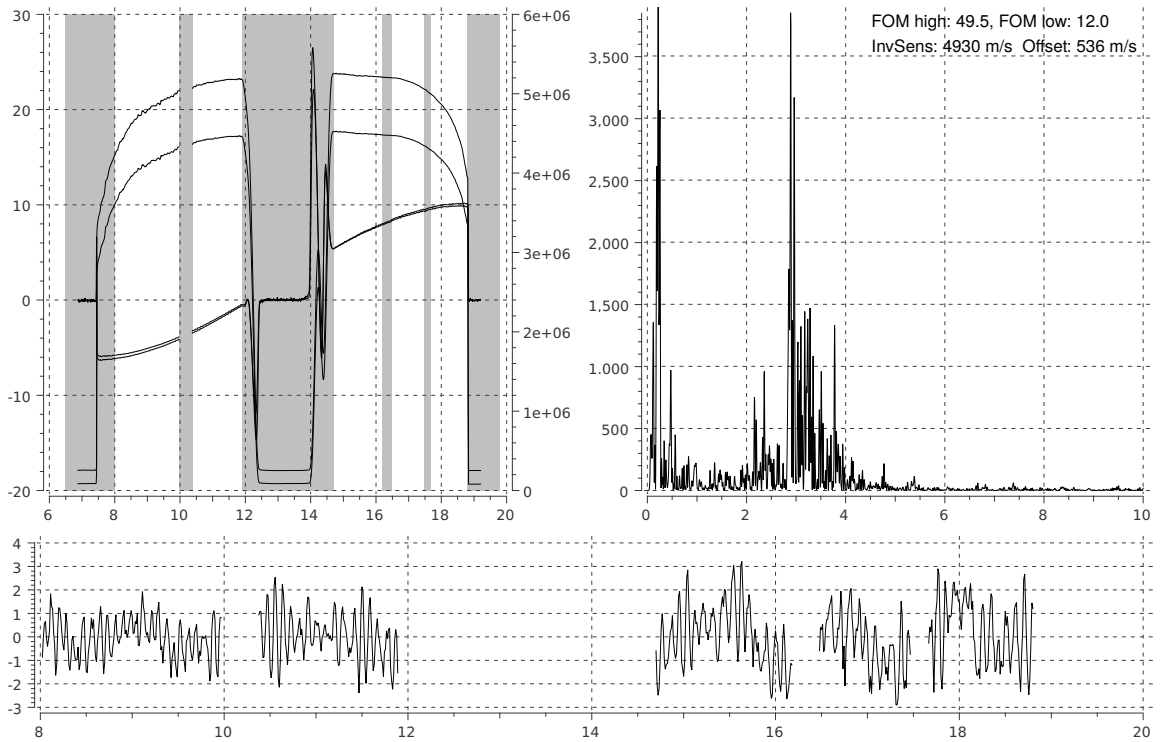
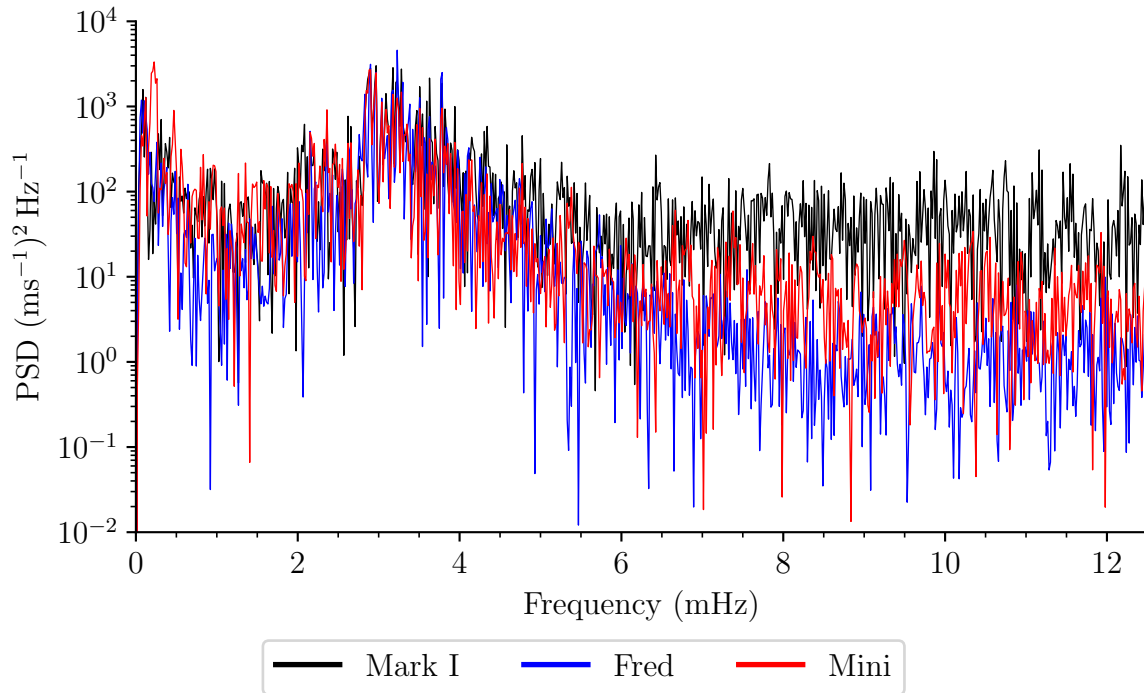**Figure 18**: 2017 September 10

Figure 19: Mark-I achieves mean noise in the $10\,\mathrm{mHz}$ to $12.5\,\mathrm{mHz}$ band of $53.6\,(\mathrm{ms}^{-1})^2\,\mathrm{Hz}^{-1}$. The new instrument achieves $6.8\,(\mathrm{ms}^{-1})^2\,\mathrm{Hz}^{-1}$. An improvement of almost a factor of 5 is still required to match the performance of Sutherland at $1.4\,(\mathrm{ms}^{-1})^2\,\mathrm{Hz}^{-1}$ on the same day.

6   Scattering PMT HV-PSU Replaced

The high-voltage power supply for the PMT failed on 2017 August 15. A spare HV-PSU was installed but with a maximum output of $2\,\mathrm{kV}$ rather than the normal $3\,\mathrm{kV}$. Since the PMT supply voltage controls the PMT gain, this means Mark-I has been running with a lower than normal signal-to-noise ratio.

The original supply was an Ortec 456 capable of supplying $3\,\mathrm{kV}$ at $10\,\mathrm{mA}$. An identical replacement spare supply was sourced at Birmingham and shipped out to Izaña. The new PSU was installed at 17:30 on 2017 September 7, returning the PMT to $3\,\mathrm{kV}$ operation. The counts from Mark-I increased from 1.1×10^6 counts to 1.3×10^6 counts, an increase of $18\,\%$.

The identical Ortec 456 was not quite as identical as expected. Each 456 has two SHV outputs on the rear panel, and on the original PSU these were both female SHV connectors. The replacement was fitted with two male SHV connectors. Examination of a third failed 456 supply revealed one male and one female SHV connector on the rear panel. In order to use the replacement PSU, it had to be disassembled and one of the male SHV connectors replaced with a female SHV connector salvaged from one of the broken HV-PSU units.

References

[1] HALE, S. J. Fibre-feed tests at Izaña in 2017 May. *BiSON Technical Report Series,* Number 384, High-Resolution Optical-Spectroscopy Group, University of Birmingham, UK, 2017. URL http://epapers.bham.ac.uk/3135/. [page 2]

[2] *ADS1210/11 24-bit Analog-to-Digital Converter.* Texas Instruments Inc., 1996. URL http://www.ti.com/lit/ds/symlink/ads1211.pdf. Revised 2005. [page 2]

[3] BAKER, B. How delta-sigma ADCs work, Part 1. Data Acquisition SLYT423A, Texas Instruments Inc., 2011. URL `http://www.ti.com/lit/an/slyt423a/slyt423a.pdf`. [page 5]

[4] BAKER, B. How delta-sigma ADCs work, Part 2. Data Acquisition SLYT438, Texas Instruments Inc., 2011. URL `http://www.ti.com/lit/an/slyt438/slyt438.pdf`. [page 5]

[5] STELLA ROBOTIC OBSERVATORY. Environmental Status (Dust). 2017. URL `http://stella.aip.de/stella/status/getdetail.php?typ=24`. [page 6]

[6] SIGRIST PROCESS-PHOTOMETER. VisGuard 2 In-situ Visibility Monitor. 2017. URL `https://classic.photometer.com/en/products/details/specification.html?productid=280`. [page 6]

[7] SIGRIST PROCESS-PHOTOMETER. SIGRIST Visibility Measurement Glossary. 2017. URL `https://www.photometer.com/en/Traffic-Environment/Visibility-Measurement/`. [page 9]

[8] HALE, S. J., CHAPLIN, W. J., DAVIES, G. R., ELSWORTH, Y. P., HOWE, R., ET AL. Atmospheric Extinction Coefficients in the I_c Band for Several Major International Observatories: Results from the BiSON Telescopes, 1984–2016. *The Astronomical Journal*, **154**(3):89, 2017. URL `https://doi.org/10.3847/1538-3881/aa81d0`. [page 9]

[9] HALE, S. J., HOWE, R., CHAPLIN, W. J., DAVIES, G. R., AND ELSWORTH, Y. P. Performance of the Birmingham Solar-Oscillations Network (BiSON). Sol. Phys., **291**(1):1–28, 2016. ISSN 1573-093X. doi:10.1007/s11207-015-0810-0. URL `https://doi.org/10.1007/s11207-015-0810-0`. [page 10]

[10] PRESS, W. H., FLANNERY, B. P., TEUKOLSKY, S. A., AND VETTERLING, W. T. *Numerical Recipes in C++: The Art of Scientific Computing*. Cambridge University Press, Cambridge, second edition, 2002. ISBN 0-521-75033-4. [page 10]

[11] COOLEY, J. W. AND TURKEY, J. W. An algorithm for the machine calculation of complex Fourier series. *Math. Comput.*, **19**:297–301, 1965. doi:10.1090/S0025-5718-1965-0178586-1. URL `https://doi.org/10.1090/S0025-5718-1965-0178586-1`. [page 10]